Epitaxial Transitions among FCC, HCP, BCC, and Cylinder Phases in a Block Copolymer Solution

Moon Jeong Park,[†,§] Joona Bang,[†] Tamotsu Harada,[†] Kookheon Char,[*,§] and Timothy P. Lodge[*,†,‡]

Department of Chemical Engineering & Materials Science and Department of Chemistry, University of Minnesota, Minneapolis, Minnesota 55455, and School of Chemical Engineering & Institute of Chemical Processes, Seoul National University, Seoul 151-744, Korea

Received April 13, 2004; Revised Manuscript Received September 4, 2004

ABSTRACT: A single concentration solution (36 vol %) of a symmetric polystyrene-*block*-polyisoprene, total molecular weight 30 000, in the styrene-selective solvent diethyl phthalate shows a remarkably rich sequence of thermotropic order−order transitions (OOT). A combination of small-angle X-ray scattering measurements both under quiescent conditions and after shear orientation, supplemented with rheology and static birefringence, indicates the following phase sequence. At room temperature the solution adopts a close-packed lattice of spherical micelles, corresponding to a mixture of face-centered-cubic (fcc) and hexagonally close-packed (hcp) phases. At approximately 60 °C the solution undergoes a "partial" OOT, in that the fcc portion transforms to body-centered-cubic (bcc), whereas the hcp domains persist. At approximately 82 °C the hcp/bcc mixture transforms to hexagonally packed cylinders, and finally the cylinder phase undergoes the order−disorder transition at 113 °C. Through the use of two different shear cells, scattering patterns along both shear gradient and vorticity axes were obtained. These data confirmed that all three OOTs (fcc to bcc, bcc to cylinder, and hcp to cylinder) are epitaxial. The first two follow the pathways previously established, whereas the hcp to cylinder is described for the first time in block copolymers. Among the other novel features of this system are the proximity to a triple line (coexistence of hcp, bcc, and cylinders) at 82 °C.

Introduction

Block copolymers belong to a broad class of compounds that can self-assemble into ordered phases with periodic microstructures.[1−3] Surfactants,[4,5] liquid crystals,[6,7] and colloids[8,9] also fall in this category of materials. The addition of a selective solvent to a block copolymer can significantly expand the range of accessible self-assembled morphologies, and under appropriate conditions of temperature and concentration, the self-assembly can produce long-range order. For instance, McConnell et al. investigated both body-centered-cubic lattice (bcc) and face-centered-cubic (fcc) micellar crystals for a polystyrene−polyisoprene (PS−PI) diblock copolymer in decane by varying degrees of block asymmetry,[10,11] and Hamley et al. also observed different ordered structures of poly(oxyethylene)−poly(oxybutylene) (EB) diblock copolymers in water, i.e., fcc and bcc, by changing the length of the hydrophilic chains.[12−14]

In block copolymer solutions, as the concentration is increased, the chains begin to overlap, leading to the formation of a liquid crystalline phase such as a cubic phase of spherical micelles, a hexagonal phase of rodlike micelles, or a lamellar phase. In some cases, polymorphism is also observed upon changing temperature, reflecting order−order transitions (OOTs) between two ordered phases. These phase transitions are typically dictated by a complicated interplay of energetic and entropic contributions to the free energy. The OOTs of block copolymer solutions have extensively been investigated using small-angle X-ray scattering (SAXS), small-angle neutron scattering (SANS), rheology, and/or birefringence.[15−26] For example, Sakurai et al. reported the thermoreversible OOT between bcc spheres and hexagonal cylinders for a PS−PI diblock copolymer in dioctyl phthalate (DOP)[27] with different polymer concentrations. Of particular relevance to this study, the transition between fcc and a hexagonal cylinder structure as a function of both concentration and temperature was observed in the work by Pople et al.[28,29] However, the detailed process and mechanism of the transition between a close-packed lattice of micelles, i.e., fcc and hexagonally close-packed (hcp), and cylinder phases have not been thoroughly understood, whereas the bcc/cylinder epitaxy has previously been well-documented.[30−35] Here, we report a detailed study of the thermoreversible transition between close-packed spheres and cylinders in a block copolymer solution, and the epitaxial relationship between hcp and cylinders is described.

Recently, we have presented the phase diagrams for six SI diblock copolymers in three PS-selective solvents (DBP, DEP, and DMP), one neutral solvent (DOP), and one PI-selective solvent (tetradecane).[17−19] In present study, the order−order transitions of a symmetric SI diblock copolymer in a styrene-selective solvent, diethyl phthalate, were investigated by in-situ SAXS on a shear-oriented solution. Figure 1 summarizes the phase behavior of the particular concentration of interest, 36%. At room temperature the solution is the mixture of fcc and hcp, but with increasing temperature there is a "partial" order−order transition from fcc to bcc around 60 °C, producing a solution that is a mixture of bcc and hcp. Upon further heating, both bcc and hcp transform to cylinders essentially simultaneously above 82 °C, and then the single cylinder phase disorders at 113 °C. The

[†] Department of Chemical Engineering & Materials Science, University of Minnesota.
[‡] Department of Chemistry, University of Minnesota.
[§] Seoul National University.
* Authors for correspondence: lodge@chem.umn.edu and khchar@plaza.snu.ac.kr.

10.1021/ma049285g CCC: $27.50
Published on Web 10/29/2004

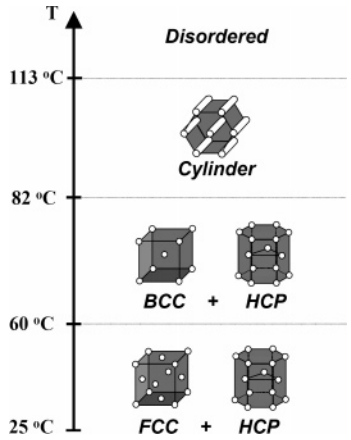

Figure 1. Phase behavior of 36% SI(15−15) in DEP showing fcc/hcp → bcc/hcp → cylinder transitions with the increase in temperature.

phase behavior bears a close resemblance to the previous results (Figure 7b in ref 18); however, the coexistence of both bcc and hcp between the fcc/hcp and cylinders is newly revealed. SAXS data were collected in two different shear cells, with the beam directed along the shear gradient direction in one and the vorticity direction in the other, to obtain a more complete picture of the three-dimensional structure.

Experimental Section

Materials. A polystyrene-*block*-polyisoprene diblock copolymer was synthesized by standard anionic polymerization procedures.[17] The block molecular weights, $M_{PS} = 15\,200$ g/mol and $M_{PI} = 15\,400$ g/mol, were determined by a combination of size-exclusion chromatography and NMR, and the sample is designated SI(15−15). The polydispersity index is 1.02. The slightly PS-selective solvent, diethyl phthalate (DEP), was obtained from Aldrich, and a solution with 36 vol % polymer was prepared using CH_2Cl_2 as a cosolvent; the CH_2Cl_2 was removed under a gentle flow of nitrogen until the solution reached constant weight. This 36% solution is specifically chosen to access all the transitions from the spheres to the cylinders as a function of temperature.

Rheology. An Advance Rheometrics Expansion System (ARES) was used to measure the dynamic storage modulus (G') and loss modulus (G'') of the 36% SI(15−15) solution in a parallel plate fixture (25 mm diameter and a ca. 0.5−1 mm gap). All measurements from 30 to 130 °C were performed in the linear viscoelastic regime with a small strain (1.0%). The temperature control was accurate to within ±1 °C, and all measurements were taken under a nitrogen atmosphere. Temperature scans were carried out at a heating rate of 0.5 °C/min and at a fixed low frequency of 0.5 rad/s. This protocol is well established as an effective means to locate OOTs and the order−disorder transition (ODT).

Static Birefringence. Static birefringence, or more correctly depolarization of a transmitted light, was also used to locate some OOTs and the ODT in this block copolymer solution. Vertically polarized light from a He−Ne laser was directed through the sample and a horizontally polarized analyzer placed before a photodiode detector. Samples in isotropic states (disordered or cubic) do not depolarize the light, and no signal is recorded, whereas lamellar or hexagonal phases are birefringent. The solution was confined between glass disks and sealed with a high-temperature adhesive and subjected to a slow temperature increase (less than 1 °C/min). Phase transitions are indicated by the abrupt appearance or disappearance of the transmitted intensity.

Quiescent Small-Angle X-ray Scattering (SAXS). Some SAXS measurements were performed at the University of Minnesota 2m beamline. Cu K_α X-rays ($\lambda = 1.542$ Å) were generated by a Rigaku RU-200BVH rotating anode, with a 0.2 × 2 mm microfocus cathode. Franks mirrors were used to focus the beam onto an area detector (Siemens HI-STAR), and the sample-to-detector distance was 2.30 m. Synchrotron SAXS measurements were also carried out at the 4C2 SAXS beamline at the Pohang Light Source (PLS) ($\lambda = 1.54$ Å and $\Delta\lambda/\lambda = 5 \times 10^{-4}$) consisting of Si (111) double crystal monochromators, ion chambers, and a two-dimensional position-sensitive detector with 1242 × 1152 pixels. The typical beam size was smaller than 1 × 1 mm^2, and the sample-to-detector distance was 2.16 m. Sample temperature was controlled within ±0.2 °C using a thermostated brass block, and at least 5 min of equilibration time was allowed at a given temperature before measurement. The resulting two-dimensional scattering images were averaged azimuthally to obtain traces of intensity vs scattering wave vector q ($q = 4\pi \sin(\theta/2)/\lambda$, where θ is the scattering angle). Solutions were sealed under an inert atmosphere in 1.5 mm quartz capillaries (Charles Supper Co.), and the capillaries were then placed in the sample holder.

In-Situ Small-Angle X-ray Scattering (SAXS). Synchrotron X-ray scattering measurements were performed using the beamline 5ID-D, in the Dupont-Northwestern-Dow (DND-CAT) synchrotron research facility at the Advanced Photon Source, Argonne National Laboratory. 17 keV radiation ($\lambda = 0.73$ Å) was selected from an undulator beam using a double-crystal monochromator, and the sample-to-detector distance was 6 m. We employed two kinds of shear cell: a Rheometrics dynamic mechanical thermal analyzer (DMTA) and a modified cone and plate. In the DMTA apertures were machined into the fixtures and covered by Kapton films with a thickness of 50 μm to allow the transmission of the X-ray beam. The "shear sandwich" parallel plate geometry has a sample thickness of 0.5 cm, and the X-ray beam passes along the shear gradient direction ($\nabla\mathbf{v}$), accessing the velocity ($\mathbf{v}$) and vorticity ($\mathbf{e}$) scattering plane, i.e., ($\mathbf{v}$, $\mathbf{e}$). The modified cone and plate shear cell was developed by Caputo and Burghardt.[36] The incident X-ray beam is directed through a hole in the fixed lower annular plate, passes through the center of the device at the virtual tip of the cone, and the sample between the annular cone and plate on the opposite side of the shear cell. In this way, the beam propagates along the vorticity direction, yielding the ($\mathbf{v}$, $\nabla\mathbf{v}$) plane. The cone angle is 5°. Since the X-ray beam is horizontal, the entire shear cell is mounted on a platform with a tilt angle of 2.5°. The inner and outer radii of the annular fixtures are 1.5 and 2.5 cm, respectively, giving a path length through the sample of 1 cm. Thin flexible heaters are glued to the faces of the fixtures opposite from the sample and are driven by a controller monitoring temperature using a thermocouple embedded in the lower plate.

Results and Discussion

To locate the OOTs as well as the ODT, three different measurements, rheology, static birefringence, and SAXS, were employed. Figure 2a shows the change of dynamic storage modulus (G') and loss modulus (G'') for the 36% SI(15−15) solution as a function of temperature. It is apparent that G' decreases abruptly at around 82 °C and then again near 113 °C. The first change signals the OOT from spheres to cylinders, and the drop at 113 °C represents the ODT. There is no obvious signature of the partial OOT from fcc to bcc spheres near 60 °C, which is consistent with the relative insensitivity of the moduli to this transition.[37,38] A more complete description of the microphase structure in each region will be developed on the basis of the SAXS measurements.

In Figure 2b, the temperature dependence of the static birefringence is presented for the same solution. The solution does not show any birefringence below 80 °C, consistent with the various sphere phases. The signal rises rapidly up to about 95 °C, where it begins to decrease. No birefringence is observed above 115 °C. Because of the anisotropy of the cylinder phase, this "off−on−off" temperature dependence on the static

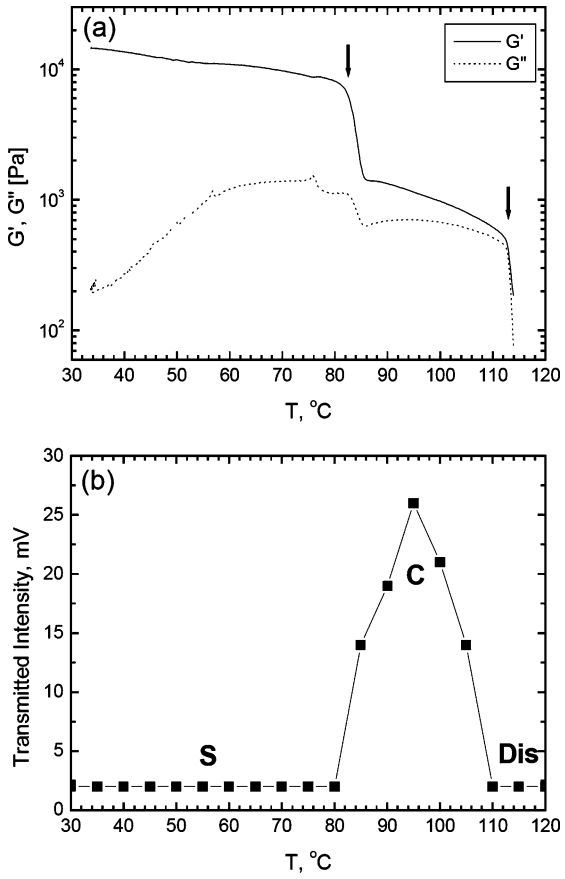

Figure 2. (a) Change of G' and G'' as a function of temperature for 36% SI(15−15) in DEP solution. Inserted arrows represent the OOT at around 82 °C and the ODT at 113 °C. A heating rate of 0.5 °C/min and frequency of 0.5 rad/s were used. (b) Static birefringence of 36% SI(15−15) in DEP as a function of temperature during heating.

birefringence is consistent with the phase sequence sphere → cylinder → disordered. (Note that the measured intensity within the cylinder phase is a complicated function of grain size, degree of segregation, etc.[17,39])

Synchrotron SAXS measurements were taken for an unoriented solution, and the azimuthally averaged intensity is plotted as a function of scattering vector q in Figure 3. Measurements were performed with a heating rate of 1 °C/min, and a further 10 min of equilibration time was allowed for every 5 °C. Since the various peaks at 30 °C are not well resolved, the peaks cannot be easily interpreted as one distinct microphase structure. The inserted arrows indicate the *expected* Bragg reflections for a mixture of fcc/hcp. Black arrows represent allowed fcc peaks with q/q^* ratios of $\sqrt{3}$:$\sqrt{4}$:$\sqrt{8}$:$\sqrt{11}$:$\sqrt{12}$:$\sqrt{16}$:$\sqrt{19}$, and white arrows show the allowed hcp peaks with ratios 1:$\sqrt{3}$:$\sqrt{4}$:$\sqrt{7}$. The coinciding arrows denote the overlap between fcc and hcp. A spherical form factor is also indicated as a dashed line in the figure, and it is noted that the form factor minimum reduces the intensities of fcc ($\sqrt{8}$) and hcp ($\sqrt{3}$) peaks. The form factor showing oscillations with minima near 0.39 and 0.68 nm^{-1} was calculated with a micelle core radius of ca. 11 nm, which was estimated from the q^* value assuming all the chains are incorporated into the micelles. However, upon heating the scattering profile changes, and at 60 °C well-separated higher-order peaks plus a low-q shoulder in the first

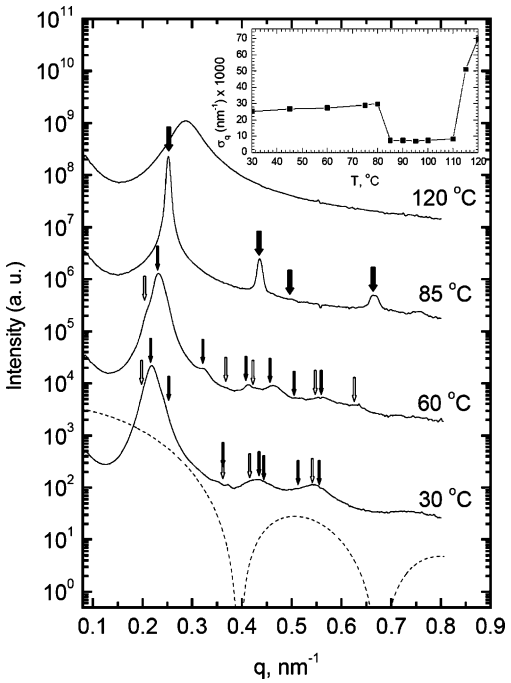

Figure 3. SAXS profiles for 36% SI(15−15) in DEP with increasing temperature. At 30 and 60 °C, black arrows represent fcc peaks and bcc peaks, respectively, while white arrows show hcp peaks. The coinciding arrows at 30 °C denote the overlap between fcc and hcp. For 85 °C, the thick arrows indicate high-order peaks with the ratio of 1:$\sqrt{3}$:$\sqrt{4}$:$\sqrt{7}$ corresponding to the cylinder phase. The dashed line corresponds to a spherical form factor for R = 11 nm: $P(q,R) = [3(\sin(qR) - (qR)\cos(qR)/(qR)^3)]^2$. The peak full width at half-maximum of the first-order peak is also shown in the inset to show the OOT and ODT clearly.

peak are observed. This scattering profile can be attributed to a mixture of bcc and hcp. The black arrows represent allowed bcc reflections with q/q^* ratios of 1: $\sqrt{2}$:$\sqrt{3}$:$\sqrt{4}$:$\sqrt{5}$:$\sqrt{6}$ while the white arrows show the same hcp peaks as at 30 °C.

At a temperature of 85 °C, the high-order peaks corresponding to $\sqrt{3}$ and $\sqrt{7}$ are clearly observed. The $\sqrt{4}$ q^* reflection is relatively weak due to the coincident extinction with the cylinder form factor. Furthermore, the full width at half-maximum of the first-order peak σ_q decreases abruptly between 80 and 85 °C, as shown in the inset. Consequently, T_{OOT} is located between 80 and 85 °C, which is also in good agreement with the rheology and birefringence data given in Figure 2. Between 110 and 115 °C σ_q rises very sharply, signaling the T_{ODT} for this solution. The SAXS profile at 120 °C confirms the presence of a disordered solution, as illustrated in Figure 3.

Coexisting FCC and HCP. To further characterize the structural changes associated with the various OOTs, SAXS experiments were conducted on shear-aligned samples, and the 2D SAXS patterns were monitored at various temperatures. The scattering pattern in the (**v**, **e**) plane obtained at 30 °C after applying a shear strain of 50% at a shear frequency of 1 rad/s for 2 h is illustrated in Figure 4a. It shows a clear hexagonal symmetry extending up to eight orders of reflections, q^*, $\sqrt{3}q^*$, $\sqrt{4}q^*$, $\sqrt{7}q^*$, $\sqrt{9}q^*$, $\sqrt{11}q^*$, $\sqrt{12}q^*$, $\sqrt{16}q^*$, where $q^* = 2\pi/d_{hcp}$ with d_{hcp} = 305 Å. This scattering pattern is characteristic of shear-oriented close-packed colloidal or micellar systems,

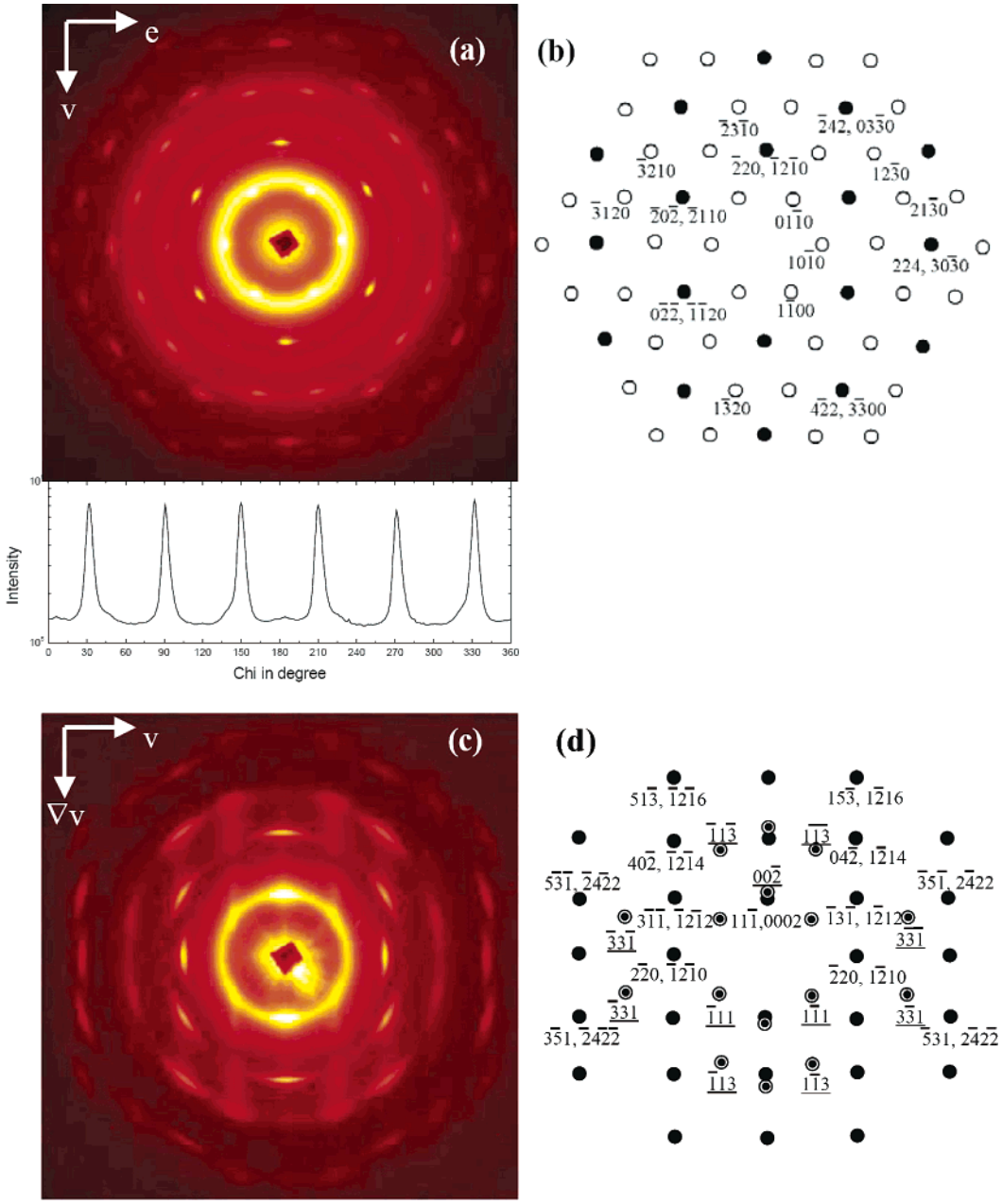

Figure 4. 2D SAXS patterns obtained from 36% SI(15−15) in DEP at 30 °C with the X-ray beam directed along (a) the shear gradient direction and (c) the vorticity direction. (b) Indexing the scattering pattern in the (**v**, **e**) plane by the combination of a crystallographic projection of the fcc crystal in the [11$\bar{1}$] beam direction and of the hcp crystal in the [0001] beam direction. The white circles indicate the hcp reflections, and the black circles denote the overlap between the fcc and the hcp reflections. (d) Indexing the scattering pattern in the (**v**, ∇**v**) plane by the combination of a crystallographic projection of the fcc/hcp crystals in the [112]/[10$\bar{1}$0] beam directions (black circles). The fcc crystal in the [110] beam direction is also indexed with underlines (white circles with black inner dots).

which has previously been documented extensively.[10,40−44] The shearing of close-packed spheres generally produces a mixture of fcc (i.e., ABCABC...) and hcp (i.e., ABABAB...) packing of the close-packed {111} planes along the shear gradient direction. The inner six spots are in fact due to the hcp stacking since there is no inner ring intensity for the perfect fcc crystal viewed along this direction. As a result, the inner six spots correspond to the {10$\bar{1}$0} planes of the hcp structure, whereas the second-order spots arise from the {220} planes of the fcc crystal as well as the {11$\bar{2}$0} planes of hcp. This assignment is identical to that presented on similar SI solutions previously.[37,45] Figure 4b provides a definitive assignment of the coexistence of both fcc and hcp structures. The white circles show the crystallographic projection of the hcp crystal in the [0001] beam direction, and the black circles denote the overlaps between fcc reflections along the [11$\bar{1}$] beam direction and hcp reflections for the [0001] beam direction.

The same solution was also examined in the modified cone and plate shear cell with the incident X-ray beam propagating along the vorticity direction, yielding the (**v**, ∇**v**) scattering plane. The scattering pattern obtained at 30 °C after the same shear conditions as Figure 4a is presented in Figure 4c. Figure 4c corresponds to a superposition of fcc and hcp SAXS patterns in the [112] and [10$\bar{1}$0] beam directions, respectively, with $\{111\}_{fcc}$ (or $\{0001\}_{hcp}$) planes oriented along the shear direction. Since these two crystals give the same scattering pattern along the vorticity direction, we can index

Figure 4c as the overlap of fcc and hcp reflections as illustrated in Figure 4d by black circles. Another notable feature is the observation of four additional spots in the inner ring (and some corresponding higher order peaks), which are attributable to {111} reflections from a fcc phase oriented at ±55° relative to the shear plane. These spots have about 15% of the intensity of the main reflections, and the probable reasons for misalignment are the inhomogeneous flow profile at the edges of the shear cell as well as the fcc stacking faults. We can assign this scattering pattern as fcc crystals viewed along the [110] direction, denoted as white circles with black inner dots in Figure 4d. Figure 4d, which reflects the combination of these three projections, gives good agreement with the experimental data shown in Figure 4c.

In general, it is difficult to distinguish which state, either fcc or hcp, is the equilibrium state, particularly when the system is subject to external fields such as shear; certainly the free energies of the two states cannot be very different for block copolymer micelles.[46,47] Besides, the ordered phase at 30 °C prior to shear alignment was not clearly determined, as indicated in Figure 3, although the profile is consistent with the cp phase. It had been reported that colloidal hard spheres favor fcc crystals among the various cp structures.[48] Since the free energy difference between cp phases is actually quite small (i.e., the Helmholtz free energies of fcc and hcp crystals differ by less than 0.05%), a significant fraction of stacking faults is often observed.[49,50] Petukhov et al. note that a random hcp (rhcp) structure is often observed when fcc might otherwise be expected, either as a long-lived transient state or stabilized by other factors such as polydispersity.[50] In an analogy to Pusey et al.,[51] we believe that there is no clear reason to expect strong correlation between n and $n + 2$ layers for hard spheres. Consequently, we postulate that the cp crystal without shear could adopt a "random" stacking sequence.[51] It is thus believed that the Bragg reflections are smeared out as shown in Figure 3 presumably due to the irregular stacking of hexagonal layers in three possible lateral positions.

The most interesting aspect lies in the fact that shearing the solution for alignment has a profound effect on the development of the hcp phase as shown in higher-order peaks for the hcp phase in Figure 4a,c, implying that the nonequilibrium shear deformation favors the formation of the hcp structure. Once the hcp phase is formed upon applying shear, it persists for a long time, and in this situation it is difficult to determine which state is the true equilibrium state. This is consistent with recent results[49,51] that the deformation of hard-sphere crystals changes the relative stability of fcc and hcp crystals. The molecular dynamics simulation for the cp structures performed by Pronk and Frenkel[52] shows that a deformation of 1.2% is enough to make the hcp phase more stable than the fcc phase. As a consequence, the free energy difference between the fcc phase and the hcp phase increases with the increase in the degree of deformation. It should be noted here that we applied a shear strain of 50%, which is sufficient to make the hcp more stable than the fcc.

To access the equilibrium state, we performed quenching measurements from the disordered state (130 °C) to erase all the previous thermal history. Figure 5 shows the scattering profile obtained shortly after quenching

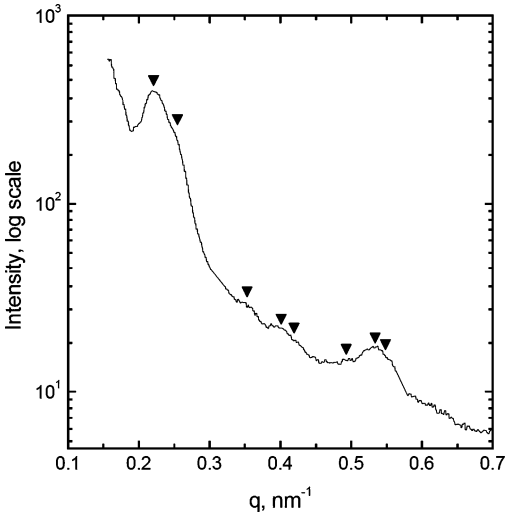

Figure 5. SAXS profile of a 36% SI(15−15) in DEP upon quenching from the disordered state (130 °C) to the 30 °C, which clearly shows fcc phase with a peak ratio of $\sqrt{3}$:$\sqrt{4}$:$\sqrt{8}$:$\sqrt{11}$:$\sqrt{12}$:$\sqrt{16}$:$\sqrt{19}$:$\sqrt{20}$.

to 30 °C from 130 °C. Noticeably, it rapidly induces a well-developed fcc phase with a ratio of $\sqrt{3}$:$\sqrt{4}$:$\sqrt{8}$:$\sqrt{11}$:$\sqrt{12}$:$\sqrt{16}$:$\sqrt{19}$:$\sqrt{20}$. This state persists for 7 h, and then it recovers the same profile as shown in Figure 3 with Bragg reflections rather smeared out. In terms of the intensities of SAXS reflections during quenching, we observed that the scattered intensity increases abruptly immediately after the quenching, and then the intensity reaches a constant value after a few hours of annealing. However, upon extended isothermal annealing for more than 6 h the scattering intensity significantly decreases concurrently with the development of the hcp phase and/or randomly close-packed spheres. This suggests that the coexisting cp phases are not due to the difference in kinetics, i.e., the disordered state partially transforms into the fcc with the remainder transforming into the hcp with slower kinetics, since in that case it is expected that the scattered intensity should continue to increase with increase in the annealing time. As a result, we can infer that the fcc and the hcp phases are not exactly degenerate in terms of free energy, and the fcc phase has a slightly lower free energy than the hcp structure based on the observed single fcc phase upon quenching. However, the system eventually progresses from the single fcc to a mixed cp phase upon isothermal annealing, indicating that a significant fraction of stacking faults starts to develop. The q^* value immediately after the quench has a slightly higher value (0.0218 Å^{-1}) compared to 0.0212 Å^{-1} obtained from the cp phase in Figure 3. The calculated fcc interplane spacing is $d_{111,\mathrm{fcc}} = 288$ Å (hcp interplane spacing was 305 Å as mentioned in Figure 4). This is consistent with the fact that the distances between the close-packed planes in hcp and fcc phases are different; the spacing between hcp layers is larger than in the fcc structure.[14] We, however, note that the interdomain spacings based on $D_{\mathrm{fcc}} = \sqrt{(3/2)}d_{\mathrm{fcc}}$ and $D_{\mathrm{hcp}} = \sqrt{(4/3)}d_{\mathrm{hcp}}$ are the same as 352 Å.

Partial OOT to Coexisting BCC and HCP. After turning off the shear, the sample was heated at a rate of 1 °C/min. The shear-aligned 2D SAXS patterns in both planes, ($\mathbf{v}$, $\mathbf{e}$) and ($\mathbf{v}$, $\nabla\mathbf{v}$), are maintained up to 60 °C. However, above 60 °C, the higher-order peaks become abruptly weaker in intensity; upon further

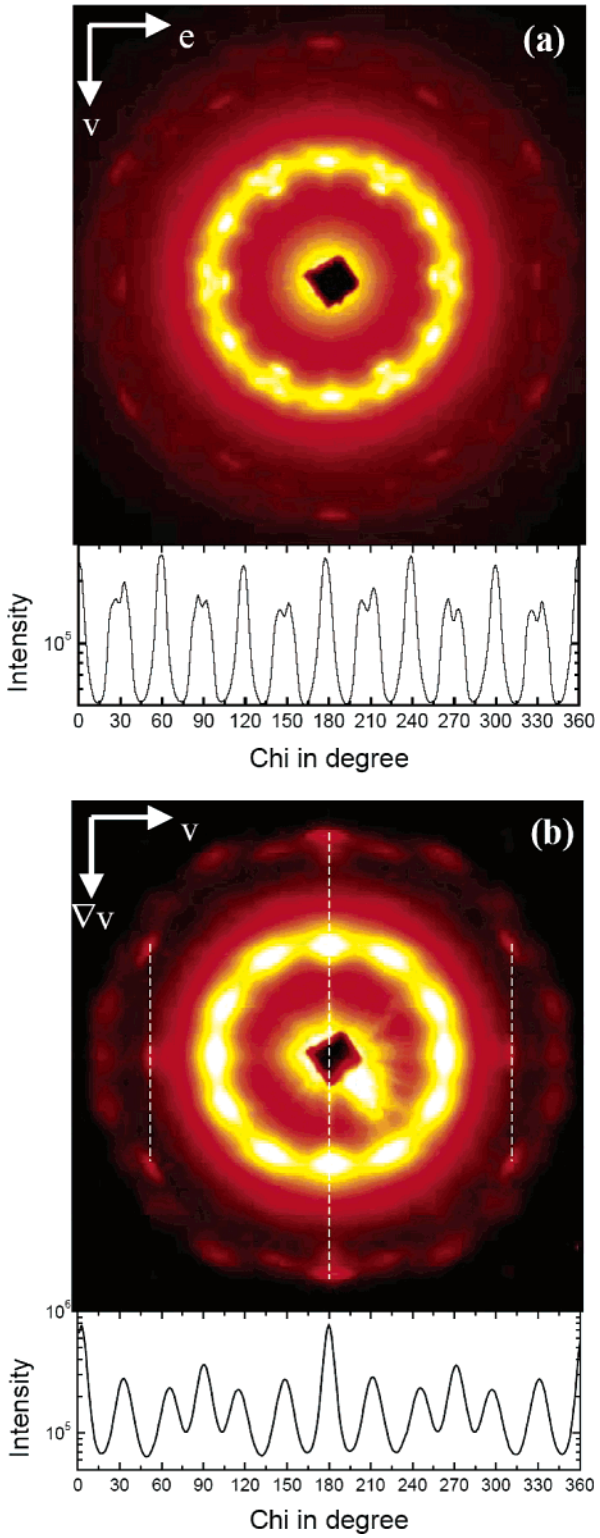

Figure 6. 2D SAXS patterns obtained from 36% SI(15−15) in DEP at 75 °C with the X-ray beam directed along (a) the shear gradient direction and (b) the vorticity direction. Azimuthal scans of the inner ring are also inserted for each figure.

heating, most of the higher-order peaks disappear, and new scattering patterns replace the six-spot pattern in the inner ring in each beam direction. Figure 6 shows a representative data set obtained at 75 °C. For the shear gradient direction (Figure 6a), the six spots in the innermost ring correspond to the $\{10\bar{1}0\}$ reflections of the hcp phase, the same as given in Figure 4a. However, 18 new spots are apparent (see the azimuthal scan; 6

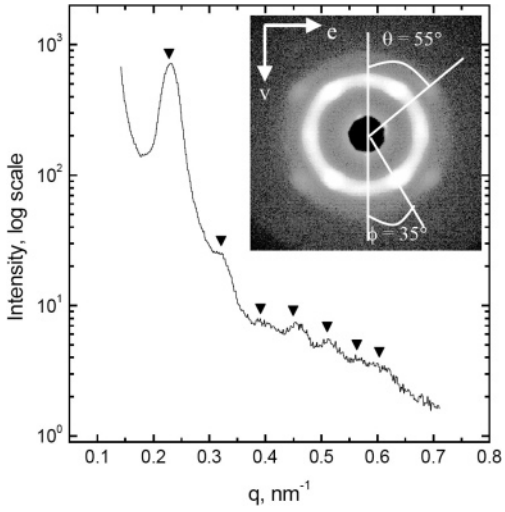

Figure 7. SAXS profile of 36% SI(15−15) in DEP upon quenching from the disordered state (130 °C) to the 75 °C. It shows a well-developed, metastable bcc phase extending up to seventh-order peak. The insert shows a 2D SAXS pattern of the twinned bcc phase obtained by applying shear immediately after the quenching.

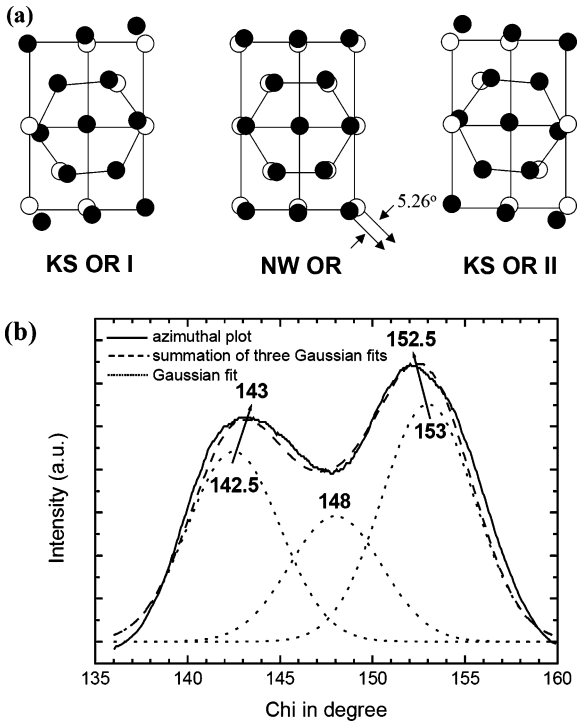

Figure 8. (a) Atomic arrangement in close-packed planes for fcc (black circles) and for bcc (white circles) as they are superimposed in two KS ORs and one NW OR. (b) Gaussian fits to the azimuthal scan of two spots as presented in Figure 6a, which clearly shows the angle difference of 10.5° between the two KS ORs and the minor contribution of the NW OR. The dotted lines show each Gaussian, and the dashed line indicates the summation of the three peaks.

at azimuthal positions of 0°, ±60°, ±120°, and 180° and 12 at 25°, 35°, 84°, 94°, 142°, 153°, 202°, 212°, 265°, 275°, 324°, 334°), indicating the emergence of a new structure. Along the vorticity direction (Figure 6b), a clear 12-spot pattern replaces the 6-spot pattern in the inner ring (see also the azimuthal scan). In Figure 6b, the remaining hcp scattering pattern is also apparent as indicated by dashed line, the same as that given in Figure 4c, and six new spots in the inner ring at azimuthal positions of ±30°, ±90°, and ±150° are also observed. The q^*

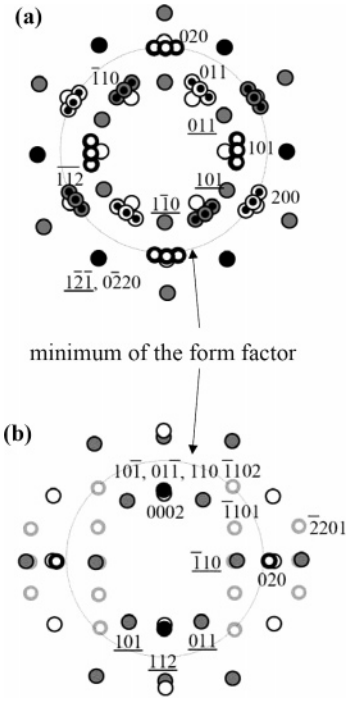

Figure 9. A definitive assignment of 2D SAXS patterns obtained from 36% SI(15−15) in DEP at 75 °C as shown in Figure 6. The diffraction patterns in (a) are from the bcc [01$\bar{1}$], [10$\bar{1}$], and [110] directions as shown with two degenerate spots: white, black, and gray circles, respectively, having an inner dot. Moreover, by considering the crystallographic projections of twinned bcc crystals (gray circles) and of hcp crystals in the [0001] beam direction (white circles), the bcc/hcp mixture can be indexed. In (b), the black circles denote the overlap of bcc crystals in the [211] and [1$\bar{1}$2] beam directions. The gray circles can be indexed by crystallographic projections of bcc crystals in [11$\bar{1}$] beam direction, and the new scattering pattern of hcp crystals in the [$\bar{1}$120] beam direction (gray circles having a white inner dot) is also observed. Black circles with inner dot and white circles indicate the bcc crystals viewed in the [101] beam direction and the hcp crystals in [10$\bar{1}$0] beam direction, respectively.

value of the hcp phase is 0.0228 Å^{-1} while that of the new phase is 0.0235 Å^{-1}.

A quench from 130 °C to the temperature of the bcc/hcp mixture was also performed. It is interesting to note that when the sample was quenched to 75 °C from 130 °C, it only shows the SAXS profile of a well-developed bcc phase extending up to the seventh-order peak, as represented in Figure 7. This state persists for 95 min, and then it recovers the same profile as Figure 3, i.e., a mixture of bcc/hcp. This behavior is reminiscent of many elemental systems[53,54] and can be viewed as an example of the Alexander and McTague conjecture[54] that bcc is predicted to be more easily accessible by rapid cooling from an isotropic liquid state for many metal systems based on entropy considerations, even when other structures, such as fcc or hcp, are lower in energy. The inset of Figure 7 shows the SAXS pattern with the X-ray beam directed along the shear gradient direction when applying a shear strain of 50% and a frequency of 1 rad/s for 1 h, directly after quenching from 130 to 75 °C. A strong 4-spot pattern in the inner ring and a weak 4-spot pattern in the outer ring with the q ratio of 1.4 are observed. This 2D scattering pattern can be explained by a highly twinned bcc structure with a 3-fold rotation axis about the [111] shear direction with flow in the {110} and {211} planes, which intersect along the same [111] direction.[55] It is interesting to note that

Table 1. Epitaxial Orientation Relationship

NW OR			
$[11\bar{1}]_{fcc}\|\|[01\bar{1}]_{bcc}$, $[101]_{fcc}\|\|[100]_{bcc}$ $[\bar{1}21]_{fcc}\|\|[011]_{bcc}$		$[101]_{fcc} \rightarrow [100]_{bcc}$	
$[11\bar{1}]_{fcc}\|\|[10\bar{1}]_{bcc}$, $[1\bar{1}0]_{fcc}\|\|[0\bar{1}0]_{bcc}$ $[112]_{fcc}\|\|[101]_{bcc}$		$[110]_{fcc} \rightarrow [100]_{bcc}$	
$[11\bar{1}]_{fcc}\|\|[110]_{bcc}$, $[011]_{fcc}\|\|[001]_{bcc}$ $[2\bar{1}1]_{fcc}\|\|[1\bar{1}0]_{bcc}$		$[011]_{fcc} \rightarrow [010]_{bcc}$	
KS OR I		KS OR II	
$[11\bar{1}]_{fcc}\|\|[01\bar{1}]_{bcc}$ $[1\bar{1}0]_{fcc}\|\|[1\bar{1}\bar{1}]_{bcc}$ $[112]_{fcc}\|\|[211]_{bcc}$	$[010]_{fcc} \rightarrow [010]_{bcc}$	$[11\bar{1}]_{fcc}\|\|[01\bar{1}]_{bcc}$ $[011]_{fcc}\|\|[111]_{bcc}$ $[2\bar{1}1]_{fcc}\|\|[2\bar{1}\bar{1}]_{bcc}$	$[\bar{1}01]_{fcc} \rightarrow [001]_{bcc}$
$[11\bar{1}]_{fcc}\|\|[10\bar{1}]_{bcc}$ $[101]_{fcc}\|\|[1\bar{1}1]_{bcc}$ $[\bar{1}21]_{fcc}\|\|[121]_{bcc}$	$[001]_{fcc} \rightarrow [001]_{bcc}$	$[11\bar{1}]_{fcc}\|\|[10\bar{1}]_{bcc}$ $[011]_{fcc}\|\|[111]_{bcc}$ $[2\bar{1}1]_{fcc}\|\|[1\bar{2}1]_{bcc}$	$[\bar{1}10]_{fcc} \rightarrow [010]_{bcc}$
$[11\bar{1}]_{fcc}\|\|[110]_{bcc}$ $[1\bar{1}0]_{fcc}\|\|[1\bar{1}\bar{1}]_{bcc}$ $[112]_{fcc}\|\|[1\bar{1}2]_{bcc}$	$[100]_{fcc} \rightarrow [100]_{bcc}$	$[11\bar{1}]_{fcc}\|\|[110]_{bcc}$ $[101]_{fcc}\|\|[1\bar{1}1]_{bcc}$ $[\bar{1}21]_{fcc}\|\|[\bar{1}12]_{bcc}$	$[01\bar{1}]_{fcc} \rightarrow [001]_{bcc}$

the azimuthal positions of the inner ring reflections (35°) are identical to those of the {110} reflections in the bcc phase, and the two pairs of off-meridional peaks in the outer ring are oriented at ±55°.[13,24,35] It is also worthwhile to note that the q^* value of 0.0235 Å^{-1} obtained after the thermal quench is the same value as the "new" phase presented in Figure 6. This confirms that the fcc → bcc transition occurs above 60 °C since the bcc phase becomes more stable than the fcc phase, and the free energy differences between the fcc and the bcc are likely to increase with further increase in temperature.

The combined SAXS patterns from two orthogonal directions, plus our recent detailed examination of the fcc to bcc transition mechanism and epitaxy,[37,45] allow a more detailed interpretation of this "partial" OOT. It is helpful to recall the well-established epitaxial relationships between fcc and bcc, which have been described in many metal systems.[56−59] In particular, orientation relationships (OR) between fcc and bcc crystals have been investigated extensively.[60−64] The three best known are the Bain, the Kurdjumov−Sachs (KS), and the Nishiyama−Wasserman (NW) ORs. Of these, the KS and NW ORs are the most frequently reported relationships for bcc−fcc systems. They reflect parallelism between the closest-packed planes, i.e., $(111)_{fcc}||(110)_{bcc}$, and they differ from each other only by a small relative rotation of 5.26°.[63,64] Figure 8a illustrates the atomic alignment in associated closed-packed planes for fcc (black circles) and bcc (white circles), superimposed as in the NW and KS ORs. For the KS OR, there are two degenerate choices; namely, the second KS OR is obtained from the first KS OR by a 10.52° in-plane rotation. Figure 8b clearly shows this angle difference of 10.5° between two KS ORs, which is obtained by fitting the azimuthal scan of two partly overlapping spots as shown in Figure 6a. The first and third dotted lines show Gaussian peak fits to the two KS ORs while the second dotted line is added by considering the NW OR. The dashed line indicates the summation of these three fits, which is in good agreement with the azimuthal scan. During the fcc-to-bcc transformation, since there are three degenerate directions for contraction (or relative slippage of neighboring close-packed planes),[37,45] a total of nine distinct orientations of the bcc unit cell (three NW and six KS ORs) can be produced. Consequently, there should be a total of 18 011 reflections for the shear gradient beam direc-

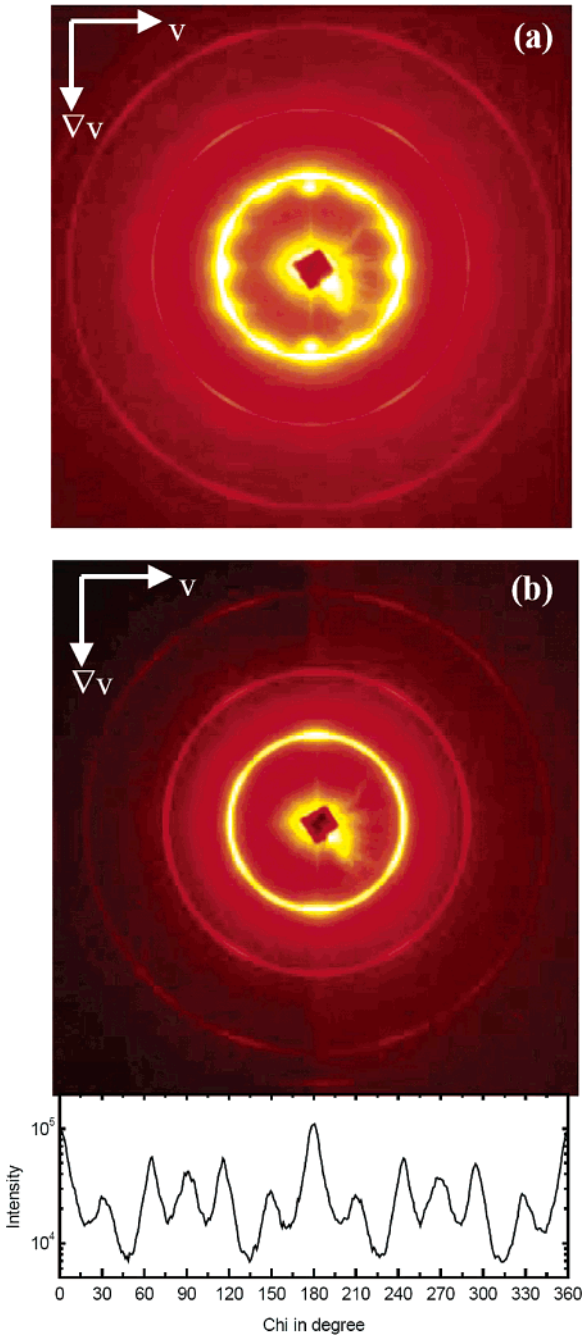

Figure 10. (a) 2D SAXS pattern obtained from 36% SI(15−15) in DEP at 82 °C with the X-ray beam directed along the vorticity direction, clearly showing the coexistence of bcc, hcp, and cylinder phases. (b) 2D SAXS pattern of the cylinder phase obtained from 36% SI(15−15) in DEP at 90 °C with the X-ray beam directed along the vorticity direction. The azimuthal scan of the inner ring shows 12 spots.

tion. In the present study we are unable to resolve a clear scattering pattern for the NW OR in the shear gradient direction; i.e., there are only 12 spots evident. However, this can also be due to the low amplitude of the NW OR, leading to only two visible spots from three different ORs, as shown in Figure 8b. As a result, the scattering pattern is indexed as a superposition of three distinct bcc crystals, viewed along the $[01\bar{1}]$, $[10\bar{1}]$, and [110] directions, as shown with three degenerated spots in Figure 9a; white, black, and gray circles, respectively, having inner dots. Table 1 summarizes all the possible bcc unit cells transformed from the fcc unit cell. (See Appendix II for the epitaxial relationship to produce the

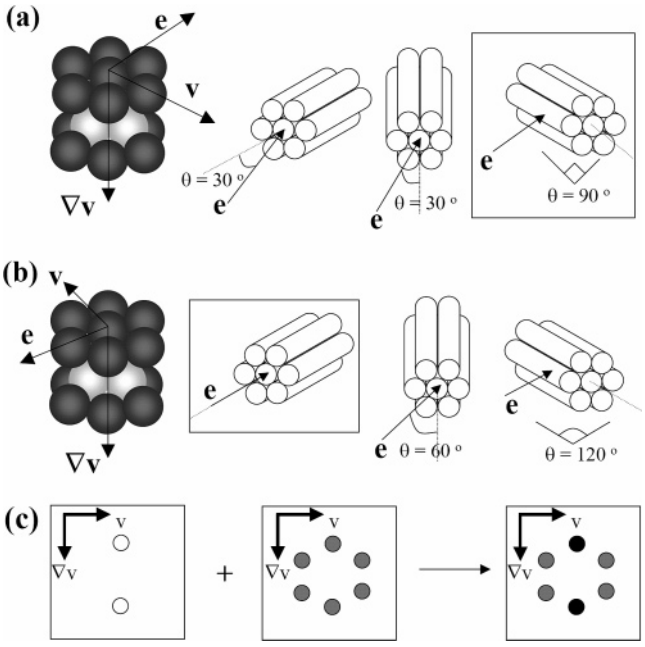

Figure 11. (a, b) The six possible cylinder axes formed by the hcp-to-cylinder transformation. (c) The $[10\bar{1}0]_{hcp} \rightarrow [001]_{cylinder}$ transition (white circles) and the $[\bar{1}\bar{1}20]_{hcp} \rightarrow [001]_{cylinder}$ transition (gray circles) yield a six-spot pattern in the ($\mathbf{v}$, $\nabla\mathbf{v}$) plane. The black circles denote the overlap between white and gray circles.

six-spot pattern as shown by gray circles at the azimuthal positions of 0°, ±60°, ±120°, and 180°.)

In the vorticity direction, as summarized in Table 1, only two bcc unit cells satisfy the ORs with the vorticity beam direction (the [112] direction in the fcc unit cell). We propose the transition from fcc in the [112] vorticity direction to bcc in [211], [101], and $[1\bar{1}2]$ directions exactly the same as in our previous study.[37,45] As presented in Figure 9b, the black circles with inner dot indicate bcc crystals viewed in the [101] beam direction while the pure black circles denote the overlap of bcc crystals in the [211], [101], and $[1\bar{1}2]$ beam directions. However, in our experimental data as shown in Figure 6b, the {110} reflections of the bcc phases were not clearly distinguished from the {0002} reflections of the hcp crystals. In addition, the scattering pattern of bcc crystals in the [101] beam direction nearby (020) hcp reflection is relatively weak. This is consistent with the indistinct center scattering spot of the three-spot patterns in shear gradient direction due to the low amplitude of the NW OR, as mentioned in Figures 6a and 8b. (See Appendix II for an additional scattering pattern not explained here; gray circles showing hexagonal symmetry as well as the rest of the gray circles having a white inner dot.)

Transition to Cylinder. Upon heating to the OOT temperature (82 °C), the 2D SAXS pattern as shown in Figure 10a clearly shows the coexistence of the bcc and hcp phases as well as new higher-order peaks with a ratio of $1:\sqrt{3}:\sqrt{7}$ due to the formation of the hexagonal cylinder phase. The cylinder peaks are distributed about distinct rings of scattering, indicating a broader (but not isotropic) distribution of cylinder orientations. Therefore, the three phases of bcc, hcp, and cylinder coexist around 82 °C. It is not possible to say definitively that this three-phase coexistence is the equilibrium state at this temperature, but certainly the phase rule allows the possibility of a triple line in this two-component

solution. We are not aware of a precedent for the experimental determination of three-phase coexistence in a block copolymer solution. Upon further slow increase in temperature, the spots corresponding to the bcc and the hcp phases gradually disappear, and the scattering pattern reduces to that equivalent to the cylinder phase only, with 12 spots in the inner ring as well as in the outer ring. These 12 spots arise from different precursors, namely the hcp and bcc phases. Figure 10b shows such a 2D SAXS pattern in the (∇**v**, **v**) plane, measured at 90 °C, with 12 clear spots in the inner ring as confirmed by the azimuthal scan. As a result, we infer there are two epitaxial order−order transitions, hcp → cylinder and bcc → cylinder. (We do not consider the scattering pattern in the (**v**, **e**) plane at 90 °C since it is too smeared due to the 10 bcc orientations. Moreover, in this plane, the cylinders grown from hcp crystals cannot give a scattering pattern in the first-order ring.)

We now examine the epitaxial relationship between the hcp and cylinder structures. Figure 11a,b shows the two existing orientations of the hcp crystal with close-packed planes in the (**e**, **v**) plane (also see Appendix II). By analogy to the bcc/cylinder transition,[30−35] we anticipate that the cylinder phase can be formed through the merging of close-packed spheres, which implies that each hcp crystal can produce three possible cylinder orientations, all lying within the (**e**, **v**) plane. Overall, there are a total of six cylinder orientations. However, only one cylinder from each set of three possible orientations can produce a perfect cylinder orientation, i.e., cylinders along a velocity direction yielding a perpendicular view from the vorticity beam direction and cylinders along a vorticity direction giving a parallel view, as indicated by the boxes shown in Figure 10a,b. For the cylinders in Figure 11a, since the vorticity direction and the cylinder axis are orthogonal, it gives a two-spot pattern at the azimuthal positions of 0° and 180° as presented by white circles in Figure 11c. For the cylinder in Figure 11b, the vorticity direction is coincident with the cylinder axis, and it clearly yields a six-spot pattern at the azimuthal positions of 0°, ±60°, ±120°, and 180° as shown by gray circles in Figure 11c. The remaining four cylinder orientations simply show the axial misorientation about the vorticity direction, yielding an azimuthal broadening of the peak intensity.[65] By the combination of these two scattering patterns, we can expect a six-spot pattern from the hcp-to-cylinder transformation, and two of them denoted by black circles in Figure 11c should be intense compared with other four spots due to the overlapping.

The epitaxial bcc → cylinder transformation is a well-known mechanism.[30−35] The (110) plane of bcc transforms into the (100) plane of cylinders, and the $[11\bar{1}]$ direction of bcc coincides with the [001] cylinder axis, as shown in Figure 12a. This transition gives another six-spot pattern at the azimuthal positions of ±30°, ±90°, and ±150° in the (**v**, ∇**v**) plane. As a result there should be a 12-spot pattern in the first ring for cylinders as shown in Figure 12c. Moreover, the intense two spots in the vertical position, symmetric four spots coming from hcp-to-cylinder transformation, and symmetric six spots by bcc-to-cylinder transitions are also consistent.

The q^* value of each ordered phase is shown in Figure 13, and each q^* value gradually increases with temperature, consistent with the decreasing interaction strength.

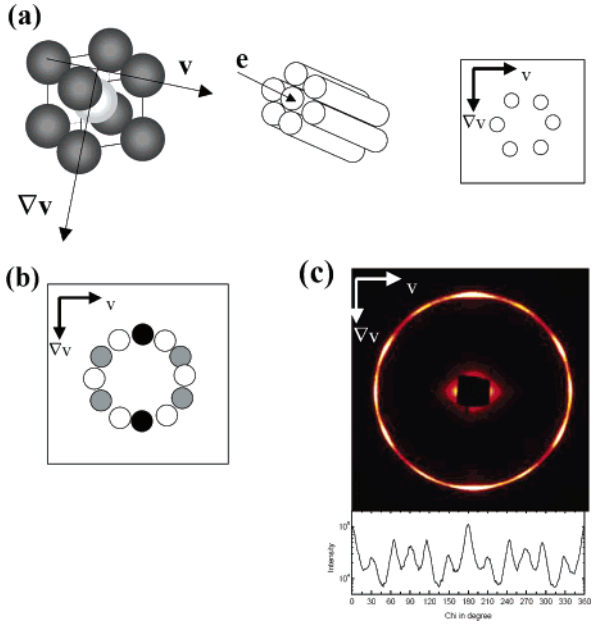

Figure 12. (a) Epitaxial $[11\bar{1}]_{bcc} \rightarrow [001]_{cylinder}$ transition and the resulting scattering pattern. By combining with the scattering pattern in Figure 11c, the 12-spot pattern can be explained very well (b), and this is in good agreement with the experimental result (c).

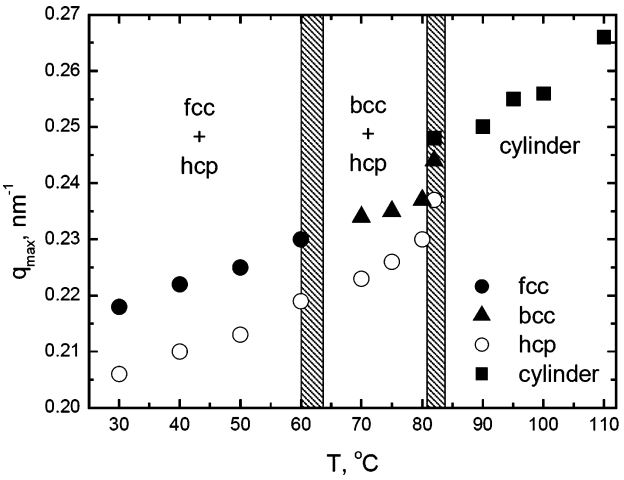

Figure 13. Change of q^* for each ordered phase as a function of temperature. The dashed zones indicate the transient region during OOT.

From the q^* value in the transition from bcc/hcp to cylinder, the interdomain spacing between the bcc microdomains (D_{bcc}) was calculated to be 315 Å (at 82 °C), that between the hcp microdomains was 306 Å (at 82 °C), and that of cylindrical microdomains ($D_{cylinder}$) was 293 Å (at 82 °C). Note that $D_{bcc} = \sqrt{(3/2)}d_{110}$ and $D_{cylinder} = \sqrt{(4/3)}d_{100}$, where d values are defined by $2\pi/q^*$. Thus, at 82 °C, the difference between D_{bcc} and $D_{cylinder}$ is about 7.5% while that between D_{hcp} and $D_{cylinder}$ is about 4.4%.

On the basis of these experimental results, we suggest the epitaxial pathway as a function of temperature for a 36% SI (15−15) diblock copolymer in DEP. At low temperature, since the energy states of the fcc and the hcp phases are quite similar, a mixture of fcc and hcp exists. However, with increasing temperature, the bcc phase becomes more stable than the fcc phase, and a mixture of bcc and hcp prevails. Upon further heating,

the bcc and hcp structures transform into the cylinder phases almost concurrently.

Conclusion

The order−order transition behavior of a PS−PI diblock copolymer in the slightly PS selective solvent, diethyl phthalate (DEP), is investigated. Three different measurements, i.e., rheology, SAXS, and static birefringence, were employed here, and the thermoreversible phase transitions of fcc/hcp → bcc/hcp → cylinder are studied. In-situ SAXS measurements with two controlled shear devices confirm the mixture of fcc and hcp crystals at room temperature, which is caused by shearing the close-packed micellar solution. Two fcc orientations and one hcp orientation are determined by indexing the SAXS data collected along the shear gradient direction as well as the vorticity direction. With the increase in temperature, unusually, the mixed fcc/hcp phase transforms into the mixture of bcc and hcp phases, and those two intermediate ordered phases are concomitantly transformed into the cylinder phase at around 82 °C. The pathway corresponds to the epitaxial transition where the cylinder axis is in line with the $[11\bar{1}]$ direction of the bcc lattice and with the $[\bar{1}\bar{1}20]$ and/or $[10\bar{1}0]$ direction of the hcp structure. On the basis of these results, we have located the epitaxial pathway among fcc, hcp, bcc, and cylinders for a symmetric SI diblock copolymer in a styrene-selective solvent, DEP.

Acknowledgment. This work was supported by the National Science Foundation through the University of Minnesota MRSEC (Award DMR-9809364). Portions of this work were performed at the DuPont-Northwestern-Dow Collaborative Access Team (DND-CAT) Synchrotron Research Center located at Sector 5 of the Advanced Photon Source. DND-CAT is supported by the E.I. DuPont de Nemours & Co., The Dow Chemical Company, the U.S. National Science Foundation through Grant DMR-9304725, and the State of Illinois through the Department of Commerce and the Board of Higher Education Grant IBHE HECA NWU 96. Use of the Advanced Photon Source was supported by the U.S. Department of Energy, Basic Energy Sciences, Office of Science, under Contract W-31-109-Eng-38. We are also grateful to the financial support from the National Research Laboratory Fund (Grant M1-0104-00-0191) by the Ministry of Science and Technology of Korea, the Brain Korea 21 Program endorsed by the Ministry of Education of Korea, and the National R&N Project for Nano Science and Technology. We appreciate use of W. R. Burghart's scattering cell.

Appendix I. Existing FCC Stacking Faults in (v, e) Plane

As we shown in Figure 4a, the fcc powder pattern in the inner ring in shear gradient direction does not disappear completely even after applying shear for 24 h. We suggest that a significant fraction of the {111} planes is not oriented parallel to the shear plane, which implies the existence of fcc stacking faults. As shown in Figure 14a, which is the azimuthal scan of the SAXS pattern measured at 30 °C with increasing shearing time, the intensity of two additional spots in the inner ring at the azimuthal positions of 0° and 180° increases. These spots are caused by the {111} planes of the fcc phase. The effect of shear was previously investigated for the EB copolymer gels.[14,42] Solutions of $E_{40}B_{10}$

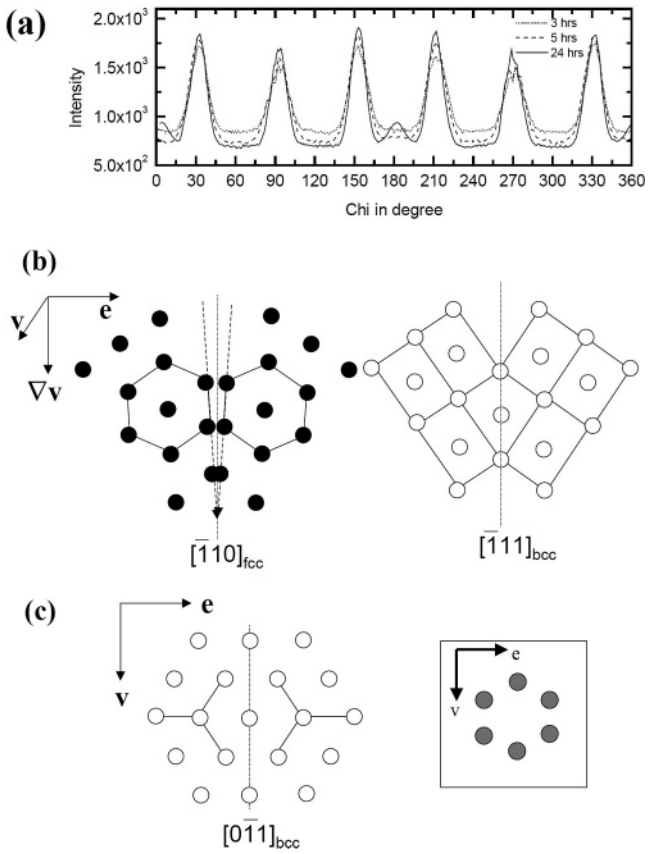

Figure 14. (a) Azimuthal scan of scattering pattern measured at 30 °C with the increase in shearing time. (b) Crystallographic projections of highly twinned fcc crystals (black circles) with a random stacking and highly twinned bcc crystals (white circles) transformed by twin fcc. (c) Inferred crystallographic projections of the twinned bcc structure in the (**v**, **e**) plane and the corresponding scattering pattern.

subjected to steady shear showed that the fcc structure forms a highly twinned structure with a random stacking of the hcp planes along the shear gradient direction. We suggest that a significant fraction of the {111} planes are oriented perpendicular to the shear plane, i.e., in the (∇**v**, **e**) planes, as illustrated in Figure 14b. These planes must then have a random stacking sequence to produce only meridional {111} reflections. Consequently, we can find the clue to the formation of another six-spot pattern in Figure 9b from this fcc stacking fault.

In the (∇**v**, **e**) planes, the fcc crystal as indicated by black circles shows a highly twinned structure, and it naturally transformed to a highly twinned bcc structure with the increase in temperature as shown by white circles. Dashed lines represent twinning boundaries. Then we can infer the crystallographic projections of the twinned bcc structure, such the (**v**, **e**) plane shown in Figure 14c. Accordingly, it produces a symmetric hexagonal pattern of (110) reflections, which is consistent with the six-spot pattern in Figures 6a and 9b.

Appendix II. The Partial OOT from the Misaligned FCC in (v, ∇v) Plane

In the vorticity direction, as we mentioned in Figure 4c, a few fcc {111} planes are oriented at ±55° relative to the shear plane, i.e., the fcc (110) orientation in the (**v**, ∇**v**) plane, giving the [110] beam direction. For this misaligned fcc, the transition behavior from fcc to bcc is more clear with the 2D SAXS pattern measured at

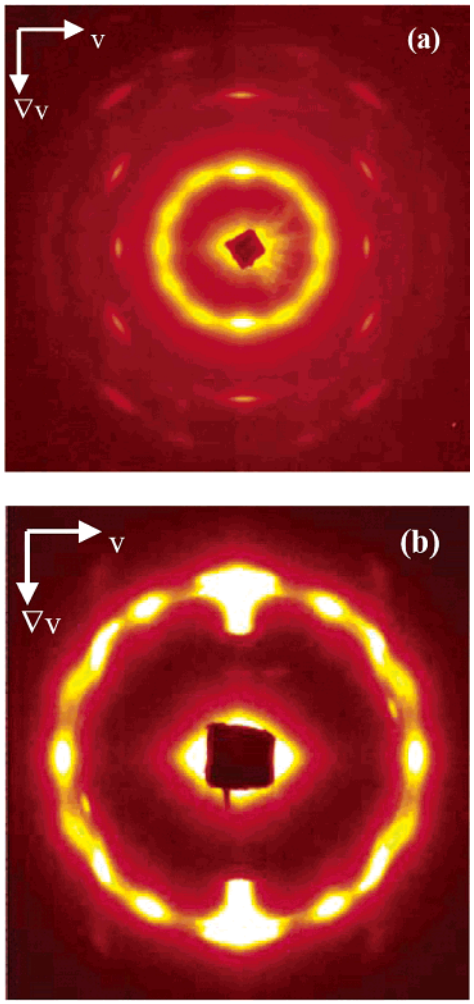

Figure 15. (a) 2D SAXS patterns obtained from a 36% SI-(15−15) in DEP solution at 65 °C with the X-ray beam directed along vorticity direction. The deformation of four spots coming from fcc {111} planes clearly shown in the magnification of inner ring (b).

65 °C, as shown in Figure 15. Noticeably, we observed the deformation of the four spots in the vorticity direction concurrently with the formation of the new six spots, as shown in Figure 15b, which is the magnification of the inner ring in Figure 15a. This implies that the structural transformation and/or deformation of the fcc phase occur at around 65 °C. For the misaligned fcc, the epitaxial relationship is in good agreement with the KS OR of $(111)_{fcc}||(110)_{bcc}$ and $[1\bar{1}0]_{fcc}||[1\bar{1}\bar{1}]_{bcc}$. As a result, the vorticity direction is in accord with the bcc $[11\bar{1}]$ direction, yielding new six spots at the azimuthal positions of ±30°, ±90°, and ±150°. In particular, for the vorticity direction, the considerable increase in the intensity of the new hcp crystal orientation, viewed along the $[\bar{1}\bar{1}20]$ beam direction as shown by gray circles having a white inner dot in Figure 9b, was observed concurrently with the formation of the bcc domains. This is the reason for the azimuthal scan result in Figure 6b; that is, the intensity of two spots at the azimuthal positions of 90° and 270° is exactly same to the summation of the intensities of new bcc and hcp domains. The reflections from $\{1\bar{1}02\}$ plane of the hcp crystal are found to be missing due to the form factor minimum as indicated in Figure 9b.

References and Notes

(1) Bates, F. S.; Fredrickson, G. H. *Annu. Rev. Phys. Chem.* **1990**, *41*, 525.
(2) Fredrickson, G. H.; Bates, F. S. *Annu. Rev. Mater. Sci.* **1996**, *26*, 501.
(3) Hamley, I. W. *The Physics of Block Copolymers*; Oxford University Press: Oxford, 1998.
(4) Seddon, J. M. *Biochim. Biophys. Acta* **1990**, *1031*, 1.
(5) Seddon, J. M.; Templer, R. H. *Philos. Trans. R. Soc. London* **1993**, *344*, 377.
(6) Pershan, P. S. *Structure of Liquid Crystal Phases*; World Scientific: Teoneck, NJ, 1998.
(7) Eiser, E.; Molino, F.; Porte, G.; Pithon, X. *Rheol. Acta* **2000**, *39*, 201.
(8) Korgel, B. A.; Fitzmaurice, D. *Phys. Rev. B* **1999**, *59*, 14191.
(9) Clarke, S. M.; Rennie, A. R. *Langmuir* **1997**, *13*, 1964.
(10) McConnell, G. A.; Lin, M. Y.; Gast, A. P. *Macromolecules* **1995**, *28*, 6754.
(11) McConnell, G. A.; Gast, A. P. *Macromolecules* **1997**, *30*, 435.
(12) Hamley, I. W.; Mortensen, K.; Yu, G.-E.; Booth, C. *Macromolecules* **1998**, *31*, 6958.
(13) Hamley, I. W.; Daniel, C.; Mingvanish, W.; Mai, S.-M.; Booth, C.; Messe, L.; Ryan, A. J. *Langmuir* **2000**, *16*, 2508.
(14) Daniel, C.; Hamley, I. W.; Mingvanish, W.; Booth, C. *Macromolecules* **2000**, *33*, 2163.
(15) Hamley, I. W.; Pople, J. A.; Gleeson, A. J.; Komanschek, B. U.; Andrews, E. T. *J. Appl. Crystallogr.* **1998**, *31*, 881.
(16) Messé, L.; Corvazier, L.; Young, R. N.; Ryan, A. J. *Langmuir* **2002**, *18*, 2564.
(17) Hanley, K. J.; Lodge, T. P.; Huang, C.-I. *Macromolecules* **2000**, *33*, 5918.
(18) Lodge, T. P.; Pudil, B.; Hanley, K. J. *Macromolecules* **2002**, *35*, 4707.
(19) Lodge, T. P.; Hanley, K. J.; Pudil, B.; Alahapperuma, V. *Macromolecules* **2003**, *36*, 816.
(20) Krishnamoorti, R.; Modi, M. A.; Tse, M. F.; Wang, H.-C. *Macromolecules* **2000**, *33*, 3810.
(21) Wang, C.-Y.; Lodge, T. P. *Macromolecules* **2002**, *35*, 6997.
(22) Lai, C.; Russel, W. B.; Register, R. A.; Marchand, G. R.; Adamson, D. H. *Macromolecules* **2000**, *33*, 3461.
(23) Lai, C.; Russel, W. B.; Register, R. A. *Macromolecules* **2002**, *35*, 841.
(24) Mortensen, K.; Theunissen, E.; Kleppinger, R.; Almdal, K.; Reynaers, H. *Macromolecules* **2002**, *35*, 7773.
(25) Alexandridis, P. *Macromolecules* **1998**, *31*, 6935.
(26) Svensson, M.; Alexandridis, P.; Linse, P. *Macromolecules* **1999**, *32*, 637.
(27) Sakurai, S.; Kawada, H.; Hashimoto, T.; Fetters, L. J. *Macromolecules* **1996**, *29*, 740.
(28) Pople, J. A.; Hamley, I. W.; Fairclough, J. P. A.; Ryan, A. J.; Komanschek, B. U.; Gleeson, A. J.; Yu, G.-E.; Booth, C. *Macromolecules* **1997**, *30*, 446.
(29) Pople, J. A.; Hamley, I. W.; Fairclough, J. P. A.; Ryan, A. J.; Komanschek, B. U.; Gleeson, A. J.; Yu, G.-E.; Booth, C. *Macromolecules* **1997**, *30*, 5721.
(30) Koppi, K. A.; Tirrell, M.; Bates, F. S.; Almdal, K.; Mortensen, K. *J. Rheol.* **1994**, *38*, 999.
(31) Ryu, C. Y.; Vigild, M. E.; Lodge, T. P. *Phys. Rev. Lett.* **1998**, *81*, 5354.
(32) Ryu, C. Y.; Lodge, T. P. *Macromolecules* **1999**, *32*, 7190.
(33) Kimishima, K.; Koga, T.; Hashimoto, T. *Macromolecules* **2000**, *33*, 968.
(34) Matsen, M. W. *J. Chem. Phys.* **2001**, *114*, 8165.
(35) Lee, H. H.; Jeong, W.-Y.; Kim, J. K. *Macromolecules* **2002**, *35*, 785.
(36) Caputo, F. E.; Burghardt, W. R. *Macromolecules* **2001**, *34*, 6684.
(37) Bang, J.; Lodge, T. P. *J. Phys. Chem. B* **2003**, *107*, 12071.
(38) Hanley, K. J. Block Copolymers: Phase Behavior in Neutral and Selective Solvents. Ph.D. Thesis, University of Minnesota, 2001.
(39) Wang, H.; Newstein, M. C.; Chang, M. Y.; Balsara, N. P.; Garetz, B. A. *Macromolecules* **2000**, *33*, 3719.
(40) Diat, O.; Porte, G.; Berret, J.-F. *Phys. Rev. B* **1996**, *54*, 14869.
(41) Chen, L. B.; Zukoski, C. F.; Ackerson, B. J.; Hanley, H. J. M.; Straty, G. C.; Barker, J.; Glinka, C. J. *Phys. Rev. Lett.* **1992**, *69*, 688.
(42) Hamley, I. W.; Pople, J. A.; Fairclough, J. P. A.; Terrill, N. J.; Ryan, A. J.; Booth, C.; Yu, G.-E.; Diat, O.; Almdal, K.; Mortensen, K.; Vigild, M. *J. Chem. Phys.* **1998**, *108*, 6929.

(43) Vigild, M. E.; Almdal, K.; Mortensen, K.; Hamley, I. W.; Fairclough, J. P. A.; Ryan, A. T. *Macromolecules* **1998**, *31*, 5702.
(44) Fairclough, J. P. A.; Ryan, A. J.; Hamley, I. W.; Li, H.; Yu, G.-E.; Booth, C. *Macromolecules* **1999**, *32*, 2058.
(45) Bang, J.; Lodge, T. P.; Wang, X.; Brinker, K. L.; Burghardt, W. R. *Phys. Rev. Lett.* **2002**, *89*, 215505.
(46) Matsen, M. W.; Bates, F. S. *Macromolecules* **1996**, *29*, 1091.
(47) Semenov, A. N. *Macromolecules* **1989**, *22*, 2849.
(48) Bolhuis, P. G.; Frenkel, D.; Mau, S.-C.; Huse, D. A. *Nature (London)* **1997**, *388*, 235.
(49) Dux, C.; Versmold, H. *Phys. Rev. Lett.* **1997**, *78*, 1811.
(50) Petukhov, A. V.; Dolbnya, I. P.; Aarts, D. G. A. L.; Vroege, G. J.; Lekkerkerker, H. N. W. *Phys. Rev. Lett.* **2003**, *90*, 028304.
(51) Pusey, P. N.; Van Megen, W.; Bartlett, P.; Ackerson, B. J.; Rarity, J. G.; Underwood, S. M. *Phys. Rev. Lett.* **1989**, *63*, 2753.
(52) Pronk, S.; Frenkel, D. *Phys. Rev. Lett.* **2003**, *90*, 028304.
(53) Mandell, M. J.; McTague, J. P.; Rahman, A. *J. Chem. Phys.* **1970**, *66*, 3070.
(54) Alexander, S.; McTague, J. P. *Phys. Rev. Lett.* **1978**, *41*, 702.
(55) Mortensen, K.; Theunissen, E.; Kleppinger, R.; Almdal, K.; Reynaers, H. *Macromolecules* **2002**, *35*, 7773.
(56) Nishiyama, Z. *Martensitic Transformation*; Academic Press: New York, 1978.
(57) Olsen, G. H.; Jesser, W. A. *Acta Metall.* **1971**, *19*, 1009.
(58) Olsen, G. H.; Jesser, W. A. *Acta Metall.* **1971**, *19*, 1299.
(59) Shimizu, K.; Nishiyama, Z. *Metall. Trans.* **1972**, *3*, 1055.
(60) Cuenya, B. R.; Doi, M.; Löbus, S.; Courths, R.; Keune, W. *Surf. Sci.* **2001**, *493*, 338.
(61) Headley, T. T.; Brooks, J. A. *Metall. Trans.* **2002**, *33*, 5.
(62) Bruce, L. A.; Jaeger, H. *Philos. Mag.* **1979**, *40*, 97.
(63) Dahmen, U. *Acta Metall.* **1982**, *30*, 63.
(64) Gotoh, Y.; Aral, I. *Jpn. J. Appl. Phys.* **1986**, *25*, L583.
(65) Honeker, C. C.; Thomas, E. L.; Albalak, R. J.; Hajduk, D. A.; Gruner, S. M.; Capel, M. C. *Macromolecules* **2000**, *33*, 9395.

MA049285G